1 **Isotopic evidence for microbial production and consumption of methane in the upper**

2 **continental crust throughout the Phanerozoic eon**

3 **Henrik Drake[1][*], Christine Heim[2], Nick M W Roberts[3], Thomas Zack[4], Mikael Tillberg[1],**

4 **Curt Broman[5], Magnus Ivarsson[6], Martin Whitehouse[7], Mats E. Åström[1]**

[1] Linnæus University, Department of Biology and Environmental Science, 39182 Kalmar, Sweden.

henrik.drake@lnu.se, mikael.tillberg@lnu.se, mats.astrom@lnu.se

5 [2] Geoscience Centre Göttingen of the Georg-August University (Department of Geobiology) Goldschmidtstr. 3,

6 37077 Göttingen, Germany. cheim@gwdg.de

7 [3] NERC Isotope Geosciences Laboratory, British Geological Survey, Nottingham, NG12 5GG, UK,

8 nirob@bgs.ac.uk

[4] Department of Earth Sciences. University of Gothenburg, 405 30 Gothenburg, Sweden. thomas.zack@gu.se

9 [5] Department of Geological Sciences, Stockholm University, 106 91 Stockholm, Sweden.

10 Curt.broman@geo.su.se

[6] Department of palaeobiology and the Nordic Center for Earth Evolution (NordCEE), Swedish Museum of

Natural History, P.O. Box 50 007, 104 05 Stockholm, Sweden. magnus.ivarsson@nrm.se

[7] Laboratory for Isotope Geology, Swedish Museum of Natural History, P.O. Box 50 007,

10405 Stockholm, Sweden. martin.whitehouse@nrm.se

*Corresponding author. Tel.; +46480 447300 Fax: +46480 447305. E-mail address: henrik.drake@lnu.se

11

12

ABSTRACT

Microorganisms produce and consume methane in terrestrial surface environments, sea sediments and, as indicated by recent discoveries, in fractured crystalline bedrock. These processes in the crystalline bedrock remain, however, unexplored both in terms of mechanisms and spatiotemporal distribution. Here we have studied these processes via a multi-method approach including microscale analysis of the stable isotope compositions of calcite and pyrite precipitated in bedrock fractures in the upper crust (down to 1.7 km) at three sites on the Baltic Shield. Microbial processes have caused an intriguing variability of the carbon isotopes in the calcites at all sites, with $\delta^{13}C$ spanning as much as -93.1‰ (related to anaerobic oxidation of methane) to +36.5‰ (related to methanogenesis). Spatiotemporal coupling between the stable isotope measurements and radiometric age determinations (micro-scale dating using new high-spatial methods: LA-ICP-MS U-Pb for calcite and Rb-Sr for calcite and co-genetic adularia) enabled unprecedented direct timing constraints of the microbial processes to several periods throughout the Phanerozoic eon, dating back to Devonian times. These events have featured variable fluid salinities and temperatures as shown by fluid inclusions in the calcites; dominantly 70-85°C brines in the Paleozoic and lower temperatures (<50-62°C) and salinities in the Mesozoic. Preserved organic compounds, including plant signatures, within the calcites mark the influence of organic matter in descending surficial fluids on the microbial processes in the fracture system, thus linking processes in the deep and surficial biosphere. These findings substantially extend the space where, and time when, production and consumption of methane within the upper continental crust is recognized.

1. Introduction

Microbial anaerobic oxidation of methane (AOM) in a variety of settings, such as marine sediments (Knittel and Boetius, 2009), the deep subseafloor biosphere (Inagaki et al., 2015; Roussel et al., 2008), fresh water wetlands (Segarra et al., 2015) and at seeps, has been suggested to occur by a syntrophic two-membered microbial consortium, consisting of: 1) anaeorobic methanotroph (ANME) *archaea;* and 2) sulfate reducing bacteria (SRB) (Michaelis et al., 2002). This phenomenon occurs at the sulfate-methane transition zone (SMTZ), a discrete depth horizon where sulfate-rich water mixes with deeper-seated methane (Knittel and Boetius, 2009), and frequently results in precipitation of calcite and pyrite from the dissolved bicarbonate and sulfide produced during AOM (Campbell et al., 2002; Peckmann and Thiel, 2004). Methane generally has carbon isotope values ($^{13}C/^{12}C$ expressed as $\delta^{13}C$) that are light (depleted in ^{13}C), especially when it is microbial (Whiticar, 1999), although significant ^{13}C-depletion has also been shown for abiotic methane of hydrothermal origin (McCollom et al., 2010), and hence, the related authigenic calcite is also commonly ^{13}C-depleted (Campbell et al., 2002; Peckmann and Thiel, 2004; Schrag et al., 2013). This calcite is therefore a frequently used tracer for AOM, in addition to diagnostic biomarkers of ANME and their SRB partner (Niemann and Elvert, 2008). Reports of fossil AOM from numerous sedimentary settings, mostly Cenozoic and rarely Mesozoic/Paleozoic (Peckmann and Thiel, 2004), show that microbial methanogenesis and oxidation have decreased the contribution of this greenhouse gas to the surface systems and atmosphere over geological eras.

In the respect of microbial methane production and consumption over Phanerozoic time scales, the vast continental crust, dominated by fractured Precambrian crystalline basement, has largely been neglected. This continental subsurface system has a total estimated biomass corresponding to up to almost 20% of the Earth's total (McMahon and Parnell,

63   2014). Pioneering investigations within the last decades confirm that microorganisms indeed

64   thrive in this oligotrophic fracture environment (Pedersen, 1997). Although microbial cell

65   densities in water filled fractures are very low (Wu et al., 2016), the vast area and surprisingly

66   high metabolic activities (Onstott et al., 2014) result in microbial mediated redox transitions

67   that significantly influence global carbon and energy fluxes (McMahon and Parnell, 2014).

68   However, the knowledge about ancient life in this vast and difficult-to-reach environment is

69   still very scarce. Basically, fractured crystalline rocks are overall untapped archives for

70   ancient organic processes and materials (Peters et al., 2016).

71   The presence of abiotic methane of deep crustal origin in fractured crystalline rocks is

72   well known (Sherwood Lollar et al., 2008), and recent observations of highly ^{13}C-depleted

73   carbonates at Laxemar, Sweden (δ^{13}C as light as -125‰ V-PDB, Drake et al., 2015) and at

74   Olkiluoto, Finland (as light as -53.8‰, Sahlstedt et al., 2016) have shown that methane has

75   been oxidised by microorganisms at several hundred meters depth in the Precambrian

76   continental crust. These carbonates have been anticipated to be relatively recently formed

77   (<10 Ma) (Drake et al., 2015; Sahlstedt et al., 2016), but no precise dating constraints have

78   yet been presented. Ongoing AOM is anticipated at these sites by contrasting depth trends of

79   methane and sulfate (Drake et al., 2015; Pedersen et al., 2008, 2014). Although the knowledge

80   of hydrogeochemical and biogeochemical (Drake et al., 2015; Sahlstedt et al., 2016) temporal

81   fluctuations in deep granitoid fracture systems have been significantly improved during recent

82   years by application of microscale isotope techniques, the AOM process in this setting is still

83   largely uncharacterised in terms of mechanisms and unknown in terms of spatiotemporal

84   extent.

85   The aim of the study was to decipher whether the recently discovered and young (<10

86   Ma) AOM- and methanogenesis-processes in fractured bedrock (Drake et al., 2015) have been

87   widespread in space and time. The spatial distribution has been assessed by extensive new

88   micro-analytical stable isotope investigations of minerals from several Precambrian

89   crystalline rock sites over large depth range (0-1700 m), and the temporal extent has been

90   targeted by utilizing new dating techniques with high spatial resolution and by focusing on

91   minerals of several generations, indicatively formed in the Paleozoic era (or later) (Drake and

92   Tullborg, 2009). These new isotope and geochronological analyses have been combined with

93   comprehensive characterisation of biomarkers (and fossilised microorganisms) and fluid

94   inclusions within the calcites, with an aim to decipher the fluid salinity and temperature as

95   well as the origin of nutrient sources related to methane formation and consumption

96   processes.

97

98   2.   **Materials and methods**

99   *2.1. Materials and sites*

100   Samples were collected from boreholes at three sites dominated by Proterozoic

101   crystalline rocks. These are Forsmark (rock crystallization age 1.89-1.86 Ga), Götemar (1.44

102   Ga) and Laxemar (1.80 Ga) in Sweden (Fig. S1). Samples of calcite (and pyrite) were taken

103   from dominantly open, but also semi-open and sealed fractures from 39 cored boreholes, one

104   outcrop and one quarry. Paragenetic minerals include fluorite, adularia K-feldspar, quartz,

105   asphaltite (Figs. 1 and S2).

106

107   *2.2. Microscale stable isotope analysis*

108   Following sample characterisation and mineral identification carried out directly on the

109   uncoated fracture surfaces using a Hitachi S-3400N SEM equipped with an integrated energy

110   dispersive spectroscopy (EDS) system under low-vacuum conditions, calcite and pyrite

111   crystals were mounted in epoxy, polished to expose crystal cross-sections and examined with

112 SEM to trace zonations. Intra-crystal SIMS-analysis (10 μm lateral beam dimension, 1-2 μm

113 depth dimension) of carbon, oxygen and sulfur isotopes were performed on a Cameca

114 IMS1280 ion microprobe. Analytical transects of up to ten analyses were made within the

115 crystals. In total 2465 analyses were made in calcite for $\delta^{13}C$ and $\delta^{18}O$ in calcite and 40 for

116 $\delta^{34}S$ of pyrite in samples with AOM-signature in the calcites. Settings follow those described

117 in Drake et al. (2015). Influence of organic carbon was avoided in the SIMS-analyses by

118 careful spot placement to areas in the crystals without micro-fractures or inclusions. The

119 uncertainty associated with potential organic inclusions and matrix composition is therefore

120 considered to be insignificant compared to the isotopic variations.

121   Calcite results are reported as per mil (‰) $\delta^{13}C$ and $\delta^{18}O$ based on the Pee Dee

122 Belemnite (V-PDB)-standard value. Several analytical sessions were carried out running

123 blocks of six unknowns bracketed by two standards. Spot transects were made from core to

124 rim within the crystals (summarised in Table 1, with full data in Table S1). Corresponding

125 analytical spots for C and O isotopes were closely placed within the crystals and analysed at

126 separate sessions.

127   Isotope data from calcite were normalised using 1) Brown Yule Marble ($\delta^{18}O$:

128 24.11±0.13‰ V-SMOW, converts to 6.55±0.13‰ V-PDB, $\delta^{13}C$: -2.28±0.08‰V-PDB,

129 derived from three replicate bulk analyses, J. Craven, Univ. of Edinburgh, pers. comm.), and

130 2) calcite standard S0161, which comes from a granulite facies marble in the Adirondack

131 Mountains, kindly provided by R.A. Stern (Univ. of Alberta). The values used for IMF

132 correction were determined by conventional stable isotope mass spectrometry at Stockholm

133 University on ten separate pieces, yielding $\delta^{13}C = -0.22 \pm 0.11$ ‰V-PDB (1 std. dev.) and

134 $\delta^{18}O = -5.62 \pm 0.11$ ‰ V-PDB (1 std. dev.) Precision was $\delta^{18}O$:±0.2-0.3‰ and $\delta^{13}C$:±0.4-

135 0.5‰.

136   Pyrite results are reported as per mil (‰) $\delta^{34}S$ based on the Canon Diablo Troilite (V-

137   CDT)-standard value. Blocks of six unknowns were bracketed by two standards (the Ruttan

138   pyrite). Analytical transects of several analyses were made from core to rim in the crystals.

139   Precision was $\delta^{34}S$ ±0.13‰.

140

141   *2.2. Micro-scale radiometric dating*

142   2.2.1. U-Pb dating

143   U-Pb geochronology is based on the two decay systems of U to Pb (^{238}U to ^{206}Pb and

144   ^{235}U to ^{207}Pb) and is commonly applied to silicate and phosphate minerals, i.e. zircon and

145   monazite, but can also be applied to carbonate minerals (see Rasbury & Cole, 2009). Using

146   the Laser Ablation Inductively Coupled Plasma Mass Spectrometry (LA-ICP-MS), which

147   allows for micro-sampling on a fine-scale, has opened up geochronology of carbonate

148   minerals to new applications (e.g. Roberts & Walker, 2016).

149   U-Pb geochronology via LA-ICP-MS was conducted at the Geochronology & Tracers

150   Facility, NERC Isotope Geosciences Laboratory (Nottingham, UK). The method utilises a

151   New Wave Research 193UC excimer laser ablation system, coupled to a Nu Instruments

152   Attom single-collector sector-field ICP-MS. The method is briefly described here and in detail

153   in the supplementary material and in Roberts and Walker (2016). The laser parameters used

154   are a 100μm static spot, ablated at 10 Hz for 30 s with a fluence of ~8 J/cm^{-2}. Material is pre-

155   ablated to clean the sample site. Normalisation uses standard sample bracketing to NIST glass

156   (for Pb/Pb ratios) and a carbonate reference material for Pb-U ratios (WC-1; see

157   supplementary material). The proposed age presented in this study was analysed alongside

158   another calcite material previously analysed by Isotope Dilution Thermal Ionisation Mass

159   Spectrometry (ID-TIMS) that can be used as a check on accuracy of the normalisation. The

160 reproducibility of the primary WC-1 reference material is around 2-4% per session. An

161 estimate of the session reproducibility is propagated (as excess variance) onto the sample

162 data. The age quoted has additional systematic uncertainties propagated onto the final age

163 (Horstwood et al., 2016), these include decay constant uncertainties, the laboratory-based

164 long-term reproducibility of the method (~2%) and the uncertainty on the reference material

165 age (~2.33%; based on in-house isotope dilution measurements).

166

167 2.2.2. Rb-Sr dating

168   The Rb-Sr dating system builds on the beta-decay of ^{87}Rb to ^{87}Sr in minerals. One or

169 several Rb-rich minerals (showing increased ^{87}Sr/^{86}Sr and decreased ^{87}Rb/^{86}Sr with time)

170 along with a co-genetic Sr-rich mineral (constant ^{87}Sr/^{86}Sr with time) are analysed and the age

171 calculated based on the decay constant. The fine-grained and zoned nature of secondary

172 minerals in crystalline-rock fractures has inhibited Rb-Sr dating using conventional

173 dissolution techniques. Here we apply Rb-Sr geochronology via a newly developed high

174 spatial resolution LA-ICP-MS method (Zack and Hogmalm, 2016), conducted at the Earth

175 Sciences Centre, University of Gothenburg, Sweden. Adularia being co-genetic with the

176 calcite analysed for stable isotopes with SIMS was searched for in detail using SEM directly

177 on the fracture surfaces. Adularia from three samples where hand-picked and mounted in

178 epoxy, polished and zonation was characterised using SEM. Discrete zones of secondary

179 adularia in paragenesis with calcite (mineral relations in Figs. 1d and S4) were then analysed

180 using micro-scale LA-ICP-MS. A brief method description is given here and a detailed in the

181 supplementary material. Separation of ^{87}Rb from ^{87}Sr is achieved by producing oxide of ^{87}Sr

182 as the ablated material reacts with N$_2$O (Hogmalm et al., 2017) or O$_2$ (Zack and Hogmalm,

183 2016) in a reaction cell sandwiched between two quadrupoles in an Agilent 8800QQQ ICP-

184 MS. N$_2$O was utilised as reaction gas for analysis of all spots in samples KFM04A:306 m,

185   KFM08A:480 m and two spots in sample KLX01:220 m, while two spots in KLX01:220 m

186   was analysed with O_2 in a separate session. $^{87}Sr/^{86}Sr$ calibration of the raw ratios of samples is

187   performed by using session-based means from repeated analysis of NIST SRM 610, which

188   had a precision of 0.19% when N_2O was utilized as reaction gas and 0.18% with O_2. Mica-Mg

189   is a pressed nanopowder pellet of a phlogopite separate that was used for $^{87}Rb/^{86}Sr$ calibration

190   and had within-run precisions of 0.85% and 1.02% with N_2O and O_2, respectively. Within-run

191   errors of standards and samples were below 2% for both $^{87}Rb/^{86}Sr$ and $^{87}Sr/^{86}Sr$ for each

192   individual spot. The $^{87}Sr/^{86}Sr$ ratios of calcite from two of the dated samples were established

193   by micro-scale MC-LA-ICP-MS analysis of the growth zone within the calcites that was in

194   paragenesis with adularia. These analyses were carried out using a Nu plasma (II) MC-ICP-

195   MS, laser ablation was done using an ESI NWR193 ArF eximer laser ablation system and the

196   analytical settings are described in detail in the supplementary material.

197

198   *2.3. Fluid inclusions*

199   Fluid inclusions were studied using microthermometry techniques for 24 samples of

200   handpicked calcite crystals (0.5-1.5 mm in size) and of calcite double-polished thin sections

201   (150 μm thick, including the same crystals analysed using SIMS). A conventional microscope

202   was used to get an outlook of the samples and the distribution of the fluid inclusions.

203   Microthermometric analyses of fluid inclusions were made with a Linkam THM 600 stage

204   mounted on a Nikon microscope utilizing a 40x long working-distance objective. The

205   working range of the stage is from -196° to +600°C (for details see Drake et al., 2015). The

206   thermocouple readings were calibrated by means of SynFlinc synthetic fluid inclusions and

207   well-defined natural inclusions in Alpine quartz. The reproducibility was ±0.1°C for

208   temperatures below 40°C and ±0.5°C for temperatures above 40°C. In total 195 inclusions

209   were measured.

210

2.4. Biomarkers

Biomarkers were analysed in extracts from 16 of the calcite samples characterised for stable

isotope composition using SIMS, and for one asphaltite sample and an alum shale reference

sample. For very small samples, calcite with similar $\delta^{13}C$-values were combined. All samples

and a sea sand blank reference sample were ground and extracted using the same

methodology described in Drake et al. (2015) and references therein. The samples were dried

with N_2, redissolved with 200µl of n-hexane and analysed with GC/MS. For the analysis of

the kerogen fraction ca 35 mg of sample extraction residues were mixed with sea sand

(glowed for 2 h at 550°C) and a molybdenum-catalyst. Catalytic hydropyrolysis (HyPy) was

conducted with a constant H flow at 5 l/min and a temperature program from 20 to 250°C for

50 min and 250 to 500°C for 8 min using a device from Strata Technology Ltd. (Nottingham,

UK). The generated pyrolysate was absorbed on silica gel in the dry ice cooled trap tube. The

HyPy pyrolysates were separated into aliphatic, aromatic and polar fractions using column

chromatography. To avoid any contamination, only pre-distilled solvents were used. All

glassware used was first glowed at 500°C. Solvent blank extracts (with pre-heated sea sand)

were performed concomitantly as contamination controls and measured together with the

investigated samples. 1µL of each sample extract (500µl) was analysed with Thermo Trace

1310 GC coupled to a Thermo TSQ Quantum Ultra triple quadrupole MS. The GC was

equipped with a fused silica capillary column (5MS, 30m lengths, 0.25mm i.d., 0.1µm film

thickness, with He as carrier gas). The temperature program of the GC oven was 80 to 310°C.

The MS source was kept at 240°C in electron impact mode at 25eV ionization energy. Most

calcites contained detectable organic matter, although in various amounts and compounds

(Tables S8). The only exception was the deepest sample. Sample KFM06C:103 contained the

most abundant organics detected with GC/MS (Table S9).

235

3. Results

The sampled calcite and pyrite dominantly occurred as euhedral crystals grown from the walls of fractures formed in an extensional stress field. The calcite coatings were up to a cm thickness and typically consisted of scalenohedral crystals (Figs. 1a-c, S2). SEM investigations of polished crystal cross-sections showed overgrowths precipitated at different events (Fig. 2d-g) and paragenetic relations between calcite-adularia and calcite-pyrite (Fig. 1d, f). Up to 10 different growth zones have been spotted (Fig. 2e) but generally they are much fewer and can, based on isotope signatures (see later sections), roughly be divided into an early phase with mm- to cm-sized crystals of scalenohedral calcite and cubic pyrite, and a later phase of calcite and pyrite overgrowths on the earlier crystals or smaller sized individual euhedral calcite crystals of various habit and pyrite crystals of cubic and framboidal habit.

The micro-scale $\delta^{13}C$ analyses showed substantial variability at all of the studied sites (Fig. 2a-c and Tables 1, S1). In total, the span was 130‰ V-PDB (site-specific spans between 60.5 and 106.8‰). Extreme ^{13}C-depletion occurred in all areas within the upper 800 m, with the minimum value as light as -70.3‰ (Forsmark), -73.9‰ (Götemar) and -93.1‰ (Laxemar). Pyrite in paragenesis with these ^{13}C-depleted calcites showed considerable range in $\delta^{34}S$ (-50.0 to +66.7‰ V-CDT; Table S2). Calcites with heavy $\delta^{13}C$ values (>0‰) were particularly frequent at the Forsmark site, generally in the upper 400 m, but also in a sample at almost 700 m, with values as heavy as +36.5‰ (Figs. 2b, S3d). The latter are to the best of our knowledge the heaviest $\delta^{13}C_{calcite}$ value ever recorded. At Laxemar, heavy $\delta^{13}C_{calcite}$ occurred at more shallow depth, 37-239 m. On the grain-level scale, intra-crystal $\delta^{13}C$-transects (Figs. 2d-g, S2) showed variations of up to 84‰ within single crystals. The formation of extremely ^{13}C-depleted calcite can overall be linked to the two major calcite precipitation phases indicated above, with paragenetic minerals presented in Table 2; the early

11

260   phase related to e.g. adularia, asphaltite and fluorite, and the later typically forming

261   overgrowths on the earlier calcite as well as generally showing heavier $\delta^{18}O_{calcite}$ (e.g. Fig. 2d-

262   g).

263   The micro-scale LA-ICP-MS Rb/Sr-dating of a Laxemar sample (KLX01:220 m) with

264    $\delta^{13}C_{calcite}$ values as light as -70.6‰ and paragenetic adularia gave a Devonian isochron age of

265   394±14 Ma (Fig. 3c, the dated calcite has similar $\delta^{18}O$ as the early phase of ^{13}C-depleted

266   calcite in Fig. 2e; paragenetic calcite-adularia relationship is shown in Figs. 1d and S4). Two

267   samples of the same paragenesis from Forsmark (KFM08A:480 m, not showing ^{13}C-depletion

268   and KFM04A:306 m with $\delta^{13}C$ values as light as -48.4‰) showed an age of 402±9 Ma that

269   overlap with the Laxemar sample and an age of 355±14 Ma slightly younger than the other

270   two, respectively (dating presented in Fig. 3a,b and Tables S4-S7, whereas SEM-

271   documentation of the paragenesis is in Fig. S4f). The heterogeneity and/or fine-grained/zoned

272   nature of these minerals inhibits conventional bulk sample dating, such as $^{40}Ar/^{39}Ar$ (Fig. S4).

273   Later overgrowths of a calcite sample from Forsmark (KFM06C:103 m), with $\delta^{13}C$ as light as

274   of -47.1‰, were dated to 173.2±7.6 Ma by micro-scale U-Pb LA-ICP-MS dating (Fig. 3d,

275   appearance in Fig. 2g). The dated crystals had very unevenly distributed U-rich zones,

276   inhibiting conventional bulk sample and isotope dilution dating techniques.

277   In the Forsmark area, the ^{13}C-enriched and ^{13}C-depleted calcites of the early phase

278   were in many fractures, but not always, related to asphaltite (Figs. 1a, S2a). The biomarker

279   analyses and the maturity of the kerogen fraction in the asphaltite analysed with catalytic

280   hydropyrolysis-GC-MS, showed n-hydrocarbon pattern (C_{14}-C_{30}), phenanthrene and its alkyl

281   derivatives and naphthalene derivatives (Figs. S5a-c) similar to an analysed reference of

282   Lower Cambrian alum shale (once covering the areas but now stripped off by erosion). In

283   addition, the calculated vitrinite reflectance (Rc for phenanthrene/methylphenanthrene, see

284   calculation in the supplementary text) of Rc=0.74-0.79 for the asphaltite is in accordance with

285   the vitrinite and graptolite reflectance (Ro=0.74-0.78) measured in a shale close by Petersen

286   et al. (2013). Primary 5-15 μm sized fluid inclusions of the early phase of calcite showed

287   homogenisation temperatures (T_h) of around 70-85°C and ice-melting temperatures equivalent

288   to brine type salinities (17-22 wt.% $CaCl_2$, Table S3 and Drake and Tullborg, 2009; detailed

289   information about the fluid inclusion studies are presented in the supplementary text). In the

290   Laxemar and Götemar areas the calcites had detectable fatty acids (such as in a ^{13}C-depleted

291   calcite from Götemar, containing $C_{16:0}$, $C_{17:0}$ai; $C_{17:0}$ and $C_{18:0}$, Table S8) but lacked the typical

292   aromatic asphaltite/shale-related biomarkers (Fig. S5). The younger calcite overgrowths in

293   Forsmark and Laxemar (e.g. Fig. 2g) showed fluid inclusion T_h of <50-62°C and salinities of

294   typically c. 2.5-8 wt.% $CaCl_2$ eq (Table S3). Preserved organic material was extracted from

295   the calcite sample of Jurassic age and showed peaks for long chain hydrocarbons >nC_{22} and

296   diterpenoid hydrocarbons like kaurene, abietadiene, ent-kaurane and dehydroabietane, which

297   are characteristic for land plants (Fig. 5; Table S9).

298

299   **4. Discussion**

300   *4.1. Calcite ages and relations to tectonic events*

301   The ages obtained for three samples of calcite-adularia of the early generation spanned

302   between 402±9 Ma and 355±14 (i.e. Fig. 3a-c) and for one calcite sample of the later phase

303   173.2±7.6 Ma (Fig. 3d) suggesting intermittent precipitation of ^{13}C-depleted and ^{13}C-enriched

304   calcite over long time periods. The $\delta^{13}C$ and $\delta^{18}O$ compositions and parageneses of the dated

305   samples are as a rule similar to the other samples with ^{13}C-depleted and ^{13}C-enriched calcite

306   that could not be dated (of both generations), indicating that the obtained ages are

307   representative for a large number of the samples. The micro-scale radiometric dating thus

308   demonstrates that the early precipitation of ^{13}C-depleted calcite in the Laxemar and Forsmark

309 areas occurred in Devonian-Carboniferous times and a later phase (the outermost parts of the

310 crystals and small discrete individual crystals) occurred in the Jurassic period. The Devonian-

311 Carboniferous ages are consistent with fracture formation and fluid circulation related to the

312 development and extension of a foreland basin (Cederbom, 2001) subsequent to the

313 Caledonian orogeny in NW Scandinavia, having a main phase at 425 to 400 Ma (Fossen and

314 Dunlap, 1998). At Götemar, determining the timing of the precipitation of the ^{13}C-depleted

315 calcites was hindered by the lack of Rb-bearing paragenetic minerals and unfavourable U/Pb

316 compositions of the calcites. Calcite and fluorite of the early precipitation phase have,

317 however, been dated previously, although not convincingly (very high MSWD and dated

318 together with fluorite grains from other areas) to 420±35 Ma (Alm et al., 2005) (and without

319 any report of $\delta^{13}C_{calcite}$).

320   In similarity with previous studies at Laxemar, the early (Paleozoic) calcite

321 dominantly has lighter $\delta^{18}O$ (e.g. the early parts of the crystals in Fig. 2e, g) than later calcite

322 (Drake and Tullborg, 2009), by a couple of per mil, but there is large variation between

323 different samples. This $\delta^{18}O$ difference can be explained by the measured temperature

324 differences between the generations (T_h: <50-62 vs 70-85°C) because if the minerals in the

325 different generations precipitated from a water with similar $\delta^{18}O$, the Paleozoic calcite should

326 be 1-5‰ lighter than the Mesozoic, when applying laboratory derived fractionation factors

327 between water and calcite (Kim and O'Neil, 1997).

328

329 *4.2. A biogenic-methane origin of the extremely ^{13}C-depleted calcites*

330   The extremely light $\delta^{13}C_{calcite}$ values point to AOM, and to a methane source of

331 biogenic origin, because such light values (in the -93 to -70‰ range) are typical for biogenic

332 methane, particularly for microbial origin (Reeburgh, 2007; Whiticar, 1999). The minimum

14

333   $\delta^{13}C_{calcite}$ values in each of the studied areas exceed the lightest value ever reported in other

334   environments (-69‰) (Campbell et al., 2002), pointing to more or less exclusive

335   incorporation of bicarbonate originating from methane, possibly due to very limited supply of

336   other carbon sources in this oligotrophic environment (Drake et al., 2015). This is in contrast

337   to observations in other highly saline and carbon-limited environments featuring heavier $\delta^{13}C$

338   values of biogenic methane (up to -35‰) than previously reported (Tazaz et al. 2013). The

339   $\delta^{34}S$ of pyrite co-genetic with the AOM-related calcites is diagnostic for bacterial sulfate

340   reduction (BSR, Fig. 4, Table S2). The very light $\delta^{34}S$ values mark BSR at high sulfate

341   concentrations at which the microbes are provided with a surplus of the required electron

342   acceptor (SO_4) and outcompete methanogenic archaea for H_2 and thus limit methanogenesis

343   (Hoehler and Alperin, 1996). The observation of increasing $\delta^{34}S_{pyrite}$ values with pyrite growth

344   (Fig. 4) reflects the fact that the $\delta^{34}S_{SO4}$ have increased with time in the decreasing sulfate

345   pool due to faster turnover of $^{32}S_{SO4}$ than $^{34}S_{SO4}$ during BSR in combination with faster

346   reduction than supply (by advection and diffusion) of sulfate, ultimately resulting in

347   superheavy pyrite-S in some fractures (up to +66.7‰, V-CDT), a common feature during

348   AOM (Borowski et al., 2013). Taken together, the superheavy S in pyrite and superlight C in

349   calcite combined with preserved SRB-specific fatty acids in the calcites (Tables S8-S9, cf.

350   Niemann and Elvert, 2008; Ziegenbalg et al., 2012) are strong support for syntrophic SRB-

351   ANME consortia which oxidised the methane, producing bicarbonate that ended up in the

352   calcites, as shown at SMTZs in other environments (Campbell et al., 2002; Knittel and

353   Boetius, 2009; Peckmann and Thiel, 2004). The two-phased fluid inclusions with T_h up to

354   62°C in the late calcite phase and even higher in the early phase supports the growth of

355   thermophilic anaerobic methane oxidising archaea, such as those found in deeply buried

356   oceanic crusts (Lever et al., 2013). It should be noted, however, that experiments on abiotic

357   synthesis of CH_4 have demonstrated isotope signatures down to -57‰, i.e. overlapping with

358   those traditionally associated with biogenic methane (Horita and Berndt, 1999; McCollom et

359   al., 2010). Hence, $\delta^{13}C_{calcite}$ values heavier than this, occurring in several of the samples with

360   ^{13}C-depleted calcite, cannot indisputably be argued to originate from biogenic methane. On

361   the other hand, the upper $\delta^{13}C$ limit of biogenic methane can be as heavy as -35‰ (Tazaz et

362   al., 2013), inhibiting certain assessment of whether the observed $\delta^{13}C_{calcite}$ values in the -57 to

363   -35‰ range originate from oxidation of abiotic or biogenic methane.

364

365   *4.3. Methanogenesis and organic-matter sources*

366   The evidence for a biogenic-methane origin of the superlight C in the calcites is

367   supported by occurrence of other calcites with very heavy C ($\delta^{13}C$ up to +36.5‰) in the

368   system (Figs. 2a, b, f). This is because the latter calcites certainly represent a residual

369   carbonate pool appearing after microbial methanogenesis that have preferentially incorporated

370   ^{12}C into the forming methane, as shown for other systems elsewhere (Budai et al., 2002;

371   Stevens and McKinley, 1995). Previous studies from the same boreholes studied here reported

372   scattered elevated methane concentrations (Fig. 6) in deep water-conducting fracture zones,

373   and high C1/(C2+C3) gas ratios supporting a microbial origin of the methane (Hallbeck and

374   Pedersen, 2009, 2012) (unfortunately, isotopic composition of the methane has not been

375   reported, and from Götemar, gases and waters have never been sampled). These waters

376   contained cultivatable autotrophic and heterotrophic methanogens suggesting that microbial

377   methanogenesis is also currently active at the sites (Hallbeck and Pedersen, 2012).

378   The spatial relation between calcite of the early phase and solid asphaltite (Figs. 1a,

379   S2a, as well as some apshaltite/shale specific biomarkers in the calcites, Table S8) in

380   Forsmark, link the methanogenesis to Lower Cambrian alum shales from which the asphaltite

381   originates. From these shales hydrocarbon mobilisation into the basement fractures in

382 Paleozoic was facilitated by elevated temperatures in the basal shale (>70°C, Sandström et al.,

383 2006) due to depression of the bedrock by several kilometres beneath a thick foreland basin

384 (Cederbom, 2001). These temperatures are in line with the T_h of the early calcite phase. The

385 highly saline inclusions of this calcite reveal the presence of a widespread continental brine in

386 the bedrock fracture volume at these times. The current groundwaters at the sites are less

387 saline (Laaksoharju et al., 2008). The input of bituminous material likely provided a nutrient

388 source for the microorganisms at Forsmark (in the form of decomposable organic-matter).

389 The overall relatively higher AOM-related $\delta^{13}C_{calcite}$ values at Forsmark than at the other sites

390 may be due to oxidation also of methane formed from thermogenic breakdown of organic

391 matter, in addition to microbial methanogenesis, which typically yield lighter $\delta^{13}C_{methane}$

392 values than those of thermogenic methane (Whiticar, 1999). A single occurrence of fossilized

393 filamentous casts of microorganisms in a vein at 300 m depth dated to 355±14 Ma is another

394 line of evidence for Paleozoic microbial activity (Figs. 2a, S7, S8). Asphaltite was not

395 observed in the Laxemar and Götemar fractures, and calcite from those areas did not contain

396 any shale-specific biomarkers. Hence, a shale source of organic C is not considered crucial for

397 methanogenesis within granite fractures, although it appears to have been the case in the

398 Forsmark area. Similar hydrocarbon infiltrations as in Forsmark have been documented in

399 numerous crystalline rock localities on all continents (Schutter, 2003).

400 The later Mesozoic AOM-related calcite overgrowths (e.g. Figs. 2g, 3d) precipitated

401 when the fractures were reactivated and circulated by less saline, colder fluids. At Forsmark,

402 the frequent spatial and textural relation between heavy $\delta^{13}C$ in calcite overgrowth and older

403 asphaltite (Fig. 1d) suggests that the methane was formed by, but not restricted to, microbial

404 degradation of the asphaltite and may explain why heavy $\delta^{13}C$ is most common in this area

405 (Fig. 2b). The fluid inclusion T_h of up to 62°C indicates formation during a period when the

406 bedrock was depressed by sedimentary rocks, which according to fission track

407   thermochronology points to Mesozoic origin (Cederbom, 2001), in line with our radiometric

408   dating. The long chain hydrocarbons and the diterpenoids in the calcite sample of Jurassic age

409   marks ancient, and previously unknown input from land plants to the deep biosphere (e.g.

410   from conifers or angiosperms, e.g. Simoneit, 1977, compounds in Fig. 5; Table S9).

411

412   *4.4.Complex spatiotemporal relationships of methanogenesis and AOM in the Phanerozoic*

413   *eon*

414   The depth distributions of the ^{13}C-enriched and -depleted calcites show that

415   methanogenesis and AOM have been scattered throughout the upper 700-800 m of the

416   bedrock through the Paleozoic-Mesozoic. Below these depths, signs of methanogenesis and

417   AOM are completely absent from the calcite record, and most $\delta^{13}C_{calcite}$ values instead point

418   towards inorganic carbon (-6.5±1.9‰). The depth restriction of AOM-related calcite to the

419   upper 800 m (Fig. 2) is in accordance with a previously reported depth limit of -730 m for

420   <10 Ma AOM-calcites at Laxemar (Drake et al., 2015). There is thus evidence that the AOM

421   process has been 1) widespread at this level (upper 800 m) in the crust and 2) intermittently

422   ongoing throughout the Phanerozoic eon under a wide range of temperatures.

423   Apart from the abrupt change at –800 m, the $\delta^{13}C_{calcite}$ values show no consistent depth

424   trends (Fig. 2a-c). In Forsmark, the abundant methanogenesis-related calcites spatially overlap

425   with the AOM-calcites, inhibiting any conclusions to be drawn about the location of any

426   ancient SMTZ. This points towards temporal variations in the depth of the SMTZ, certainly

427   related to fluctuations in the absolute and relative concentrations of dissolved sulfate and

428   methane in the waters. This is accentuated by the local-scale heterogeneity in $\delta^{13}C_{calcite}$ values.

429   For example, fractures at -35.8 m carry calcite with heavy $\delta^{13}C$ (+2.7‰) whereas two nearby

430   fractures (-36.43 and -37.08 m) carry AOM-calcite (as light as -68.5 and -70.3‰,

431 respectively). At current, the Forsmark fracture waters have high sulfate concentrations in the

432 upper 500 m (up to almost 600 mg/L, Fig. 6) and very low concentrations at greater depth

433 (~100 mg/L), and measurable elevated methane concentrations only at approximately −500 m

434 (Hallbeck and Pedersen, 2012; Laaksoharju et al., 2008). These features are consistent with

435 the fact that methanogenesis is inhibited at high sulfate concentrations (Hoehler and Alperin,

436 1996), and is evidence that the spatial distribution of sulphate and methane concentration

437 indeed have varied at this site over time.

438   At Laxemar, the current hydrochemical conditions are reverse to those at Forsmark,

439 with increasing sulfate concentrations with depth and scattered elevated methane

440 concentrations at shallower depths (Drake et al., 2015, Fig. 6). At the depths of high dissolved

441 sulfate concentrations, there is locally abundant fracture-filling gypsum related to the early

442 calcite phase (Drake and Tullborg, 2009). This suggests that high sulfate concentrations have

443 prevailed at these depths at this site for long time periods, which can explain why deep

444 methanogenesis-signatures are absent at these depths in this area. Instead, methanogenesis

445 seems to be restricted to shallow depths (37-239 m), and AOM may have occurred 1) in the

446 upper part of this depth span during inflow of sulfate rich water (cf. the light $\delta^{13}C_{calcite}$ near

447 the surface, Fig. 2a), in a manner similar to SMTZs in marine sediments (Knittel and Boetius,

448 2009, and references therein) and as indicated also by the clusters of extremely light $\delta^{13}C_{calcite}$

449 at shallow depths in both Götemar and Forsmark (Figs. 2b, c), and 2) at greater depth

450 where/when the dissolved sulfate concentrations increased due to dissolution of gypsum, in a

451 process similar to that reported for AOM at the contact to deep brine incursions in sub-

452 seafloor habitats (Parkes et al., 2005). In a manner similar to Forsmark, large depth variations

453 over time in the absolute and relative methane and sulfate concentrations between various

454 isolated water-conducting fracture zones is expected, as can be seen in the current system in

455   terms of large variations in sulfate concentrations in neighbouring fracture zones at similar

456   depths (Laaksoharju et al., 2008).

457   The extreme variability of the intra-crystal δ^{13}C-transects (Figs. 2d-g, S3) supports

458   that methanogenesis and AOM have been episodic. In Forsmark, methanogenesis- and AOM-

459   related calcite is most common in the late generation (see outer part of crystals in Figs. 2e, f)

460   but also exists in several of the crystal zones belonging to the earlier generation (Table S1,

461   Figs. S3e, f). In Laxemar the AOM-related δ^{13}C-signatures are found abundantly in both the

462   old generation (Fig. 2d, whole crystal, and early ^{13}C-depleted zone in Fig. 2e, both featuring

463   relatively light δ^{18}O) and in the latest overgrowths (outer ^{13}C-depleted part of crystal in Fig.

464   2e, with relatively heavy δ^{18}O). Apart from these periods of ^{13}C-depleted and -enriched calcite

465   precipitation there are also abundant precipitation of calcite from other C-sources, including

466   organic C, as shown by calcite with δ^{13}C in the range of -30 to 0‰, which cannot be

467   considered diagnostic for either AOM or methanogenesis without supporting evidence

468   (although abiotic methane can have heavier δ^{13}C than -30‰, Etiope and Sherwood Lollar,

469   2013). Since no crystal features both heavy and very light δ^{13}C, fracture scale interpretations

470   of temporal depth evolution of the SMTZ is inhibited.

471   Although our findings show that microbial methane formation and consumption have

472   occurred over long time frames throughout the upper 700-800 m of the crystalline continental

473   crust, these processes have obviously been episodic. Additionally, there is an abundance of

474   fracture calcite formed from other C sources (Drake and Tullborg, 2009, Sandström and

475   Tullborg, 2009), as well as calcites with δ^{13}C values in the -57 to -35‰ range have an

476   uncertain methane source. Taken together, these features make quantification of the total

477   amounts of methane produced and consumed by microorganisms in the fracture network over

478   time challenging and rather speculative. Ideally, corresponding studies in similar bedrock

479   settings on other continents would be needed to make a thorough global budget assessment.

480 Nevertheless, methane-related microbial processes were identified at all three sites studied,

481 and occurred throughout a vast bedrock volume (upper 700-800 m), and thus are potentially

482 quantitatively important and deserve thorough attention in future studies of methane sources

483 and sinks in the terrestrial environment. The 700-800 m depth seems to be a critical border

484 below which microbial methane cycling has not occurred on any time throughout the

485 Phanerozoic eon. The biomarker signatures preserved in the calcites reveal a surficial origin

486 of the organic matter that is consumed by the subsurface microbes, and the dissolved organic

487 carbon concentrations in the modern groundwaters show a significant decrease with

488 increasing depth (Laaksoharju et al., 2009). Taken together, the 700-800 m level points to a

489 terrestrial depth limit for microbial methane cycling influenced by descending surficial (or

490 sedimentary) organic matter.

491

5. Conclusions

493   This study has identified the heaviest values and largest spans in $\delta^{13}C_{calcite}$ ever

494 reported. In total a range of 129.6‰ V-PDB (-93.1 to +36.5‰) was detected within calcite

495 from the fractured granitoid rocks of the upper continental crust. We propose that the

496 astonishingly light $\delta^{13}C_{calcite}$ values formed due to incorporation of bicarbonate into the calcite

497 with biogenic methane produced by methanogens more or less as the single C-source. These

498 features are, in turn, undisputable evidence of microbial formation and consumption of

499 methane within the upper 700-800 m of the continental crust.

500   New dating methods with high spatial resolution were used to determine, for the first

501 time, direct timing of ancient methanogenesis and methane oxidation in the crystalline crust.

502 The results show that these processes date back in time at least several hundreds of millions of

503 years, covering several eras during the Phanerozoic eon. In Devonian-Carboniferous an early

504 phase of these processed occurred, in the Jurassic a later phase.

505   A biogenic origin of co-genetic pyrite supports a coupled bacterial sulphate reduction

506 – methane oxidation process in the anaerobic fracture system. Organic compounds preserved

507 within the minerals suggest a connection between the surficial and deep biospheres over

508 geological eras. Considering that vast areas of similar crust as we have studied here occur on

509 all continents of Earth, the observed processes can play an important part in carbon cycling

510 within the upper crust, and have acted as widespread sources and sinks for methane over the

511 Phanerozoic eon.

512

513 **Acknowledgements**

517

518 **Appendix A. Supplementary material**

519 Supplementary material related to this article can be found on-line.

520

521 **References**

522 Alm, E., Sundblad, K., Huhma, H., 2005. Sm-Nd isotope determinations of low-temperature

523   fluorite-calcite-galena mineralization in the margins of the Fennoscandian Shield,

524   Swedish Nuclear Fuel and Waste Management Co. (SKB), p. 58. Stockholm, Sweden.

525 Borowski, W.S., Rodriguez, N.M., Paull, C.K., Ussler Iii, W., 2013. Are [34]S-enriched

526   authigenic sulfide minerals a proxy for elevated methane flux and gas hydrates in the

527   geologic record? Marine and Petroleum Geology 43, 381-395.

528 Budai, J.M., Martini, A.M., Walter, L.M., Ku, T.C.W., 2002. Fracture-fill calcite as a record

529   of microbial methanogenesis and fluid migration; a case study from the Devonian

530   Antrim Shale, Michigan Basin. Geofluids 2, 163-183.

531 Campbell, K.A., Farmer, J.D., des Marais, D., 2002. Ancient hydrocarbon seeps from the

532   Mesozoic convergent margin of California: carbonate geochemistry, fluids and

533   palaeoenvironments. Geofluids 2, 63–94.

534 Cederbom, C., 2001. Phanerozoic, pre-Cretaceous thermotectonic events in southern Sweden

535   revealed by fission track thermochronology. Earth and Planetary Science Letters 188,

536   199-209.

537 Drake, H., Tullborg, E.-L., 2009. Paleohydrogeological events recorded by stable isotopes,

538   fluid inclusions and trace elements in fracture minerals in crystalline rock, Simpevarp

539   area, SE Sweden. Applied Geochemistry 24, 715-732.

540 Drake, H., Åström, M.E., Heim, C., Broman, C., Åström, J., Whitehouse, M.J., Ivarsson, M.,

541   Siljeström, S., Sjövall, P., 2015. Extreme ^{13}C-depletion of carbonates formed during

542   oxidation of biogenic methane in fractured granite. Nature Communications 6, 7020.

543 Etiope, G., Sherwood Lollar, B., 2013. Abiotic methane on Earth. Reviews of Geophysics 51,

544   276-299.

545 Fossen, H., Dunlap, W.J., 1998. Timing and kinematics of Caledonian thrusting and extension

546   collapse, southern Norway; evidence from [40]Ar/[39]Ar thermochronology. Journal of

547   Structural Geology 20, 765-781.

548   Hallbeck, L., Pedersen, K., 2009. Explorative analyses of microbes, colloids, and gases

549   together with microbial modelling. Site description model. SDM-Site Laxemar,

550   Swedish Nuclear Fuel and Waste Management Co. (SKB), Stockholm, Sweden.

551   Hallbeck, L., Pedersen, K., 2012. Culture-dependent comparison of microbial diversity in

552   deep granitic groundwater from two sites considered for a Swedish final repository of

553   spent nuclear fuel. FEMS Microbiology Ecology 81, 66–77.

554   Hoehler, T.M., Alperin, M.J., 1996. Anaerobic methane oxidation by a methanogen-sulfate

555   reducer consortium: geochemical evidence and biochemical considerations, in:

556   Lidstrom, M.E., Tabita, F.R. (Eds.), Microbial Growth on C_1-Compounds. Kluwer,

557   Dordrecht, pp. 326-333.

558   Hogmalm, K.J., Zack, T., Karlsson, A., Sjöqvist, A.S.L., Garbe-Schönberg, D., 2017. In situ

559   Rb-Sr and K-Ca dating by LA-ICP-MS/MS: an evaluation of N_2O and SF_6 as reaction

560   gases. Journal of Analytical Atomic Spectrometry. doi: 10.1039/C6JA00362A

561   Horita, J., Berndt, M.E., 1999. Abiogenic Methane Formation and Isotopic Fractionation

562   Under Hydrothermal Conditions. Science 285, 1055.

563   Horstwood, M.S.A., Košler, J., Gehrels, G., Jackson, S.E., McLean, N.M., Paton, C., Pearson,

564   N.J., Sircombe, K., Sylvester, P., Vermeesch, P., Bowring, J.F., Condon, D.J., Schoene,

565   B., 2016. Community-Derived Standards for LA-ICP-MS U-(Th-)Pb Geochronology –

566   Uncertainty Propagation, Age Interpretation and Data Reporting. Geostandards and

567   Geoanalytical Research 40, 311-332.

568   Inagaki, F., Hinrichs, K.U., Kubo, Y., Bowles, M.W., Heuer, V.B., Hong, W.L., Hoshino, T.,

569   Ijiri, A., Imachi, H., Ito, M., Kaneko, M., Lever, M.A., Lin, Y.S., Methé, B.A., Morita,

570   S., Morono, Y., Tanikawa, W., Bihan, M., Bowden, S.A., Elvert, M., Glombitza, C.,

571   Gross, D., Harrington, G.J., Hori, T., Li, K., Limmer, D., Liu, C.H., Murayama, M.,

572   Ohkouchi, N., Ono, S., Park, Y.S., Phillips, S.C., Prieto-Mollar, X., Purkey, M.,

573   Riedinger, N., Sanada, Y., Sauvage, J., Snyder, G., Susilawati, R., Takano, Y., Tasumi,

574   E., Terada, T., Tomaru, H., Trembath-Reichert, E., Wang, D.T., Yamada, Y., 2015.

575   Exploring deep microbial life in coal-bearing sediment down to ~2.5 km below the

576   ocean floor. Science 349, 420.

577 Kim, S.-T., O'Neil, J.R., 1997. Equilibrium and nonequilibrium oxygen isotope effects in

578   synthetic carbonates. Geochimica et Cosmochimica Acta 61, 3461-3475.

579 Knittel, K., Boetius, A., 2009. Anaerobic Oxidation of Methane: Progress with an Unknown

580   Process. Annual Review of Microbiology 63, 311-334.

581 Laaksoharju, M., Smellie, J., Tullborg, E.-L., Gimeno, M., Molinero, J., Gurban, I., Hallbeck,

582   L., 2008. Hydrogeochemical evaluation and modelling performed within the Swedish

583   site investigation programme. Applied Geochemistry 23, 1761-1795.

584 Lever, M.A., Rouxel, O., Alt, J.C., Shimizu, N., Ono, S., Coggon, R.M., Shanks, W.C.,

585   Lapham, L., Elvert, M., Prieto-Mollar, X., Hinrichs, K.-U., Inagaki, F., Teske, A., 2013.

586   Evidence for Microbial Carbon and Sulfur Cycling in Deeply Buried Ridge Flank

587   Basalt. Science 339, 1305.

588 McCollom, T.M., Lollar, B.S., Lacrampe-Couloume, G., Seewald, J.S., 2010. The influence

589   of carbon source on abiotic organic synthesis and carbon isotope fractionation under

590   hydrothermal conditions. Geochimica et Cosmochimica Acta 74, 2717-2740.

591 McMahon, S., Parnell, J., 2014. Weighing the deep continental biosphere. FEMS Microbiol

592   Ecol 87, 113-120.

593 Michaelis, W., Seifert, R., Nauhaus, K., Treude, T., Thiel, V., Blumenberg, M., Knittel, K.,

594   Gieseke, A., Peterknecht, K., Pape, T., Boetius, A., Amann, R., Jørgensen, B.B.,

595   Widdel, F., Peckmann, J., Pimenov, N.V., Gulin, M.B., 2002. Microbial reefs in the

596   Black Sea fueled by anaerobic oxidation of methane. Science 297, 1013– 1015.

597   Niemann, H., Elvert, M., 2008. Diagnostic lipid biomarker and stable carbon isotope

598   signatures of microbial communities mediating the anaerobic oxidation of methane with

599   sulphate. Organic Geochemistry 39, 1668-1677.

600   Onstott, T.C., Magnabosco, C., Aubrey, A.D., Burton, A.S., Dworkin, J.P., Elsila, J.E.,

601   Grunsfeld, S., Cao, B.H., Hein, J.E., Glavin, D.P., Kieft, T.L., Silver, B.J., Phelps, T.J.,

602   van Heerden, E., Opperman, D.J., Bada, J.L., 2014. Does aspartic acid racemization

603   constrain the depth limit of the subsurface biosphere? Geobiology 12, 1-19.

604   Parkes, R.J., Webster, G., Cragg, B.A., Weightman, A.J., Newberry, C.J., Ferdelman, T.G.,

605   Kallmeyer, J., Jørgensen, B.B., Aiello, I.W., Fry, J.C., 2005. Deep sub-seafloor

606   prokaryotes stimulated at interfaces over geological time. Nature 436, 390-394.

607   Peckmann, J., Thiel, V., 2004. Carbon cycling at ancient methane-seeps. Chemical Geology

608   205, 443-467.

609   Pedersen, K., 1997. Microbial life in granitic rock. FEMS Microbiology Rev. 20, 399-414.

610   Pedersen, K., Arlinger, J., Hallbeck, A., Hallbeck, L., Eriksson, S., Johansson, J., 2008.

611   Numbers, biomass and cultivable diversity of microbial populations related to depth and

612   borehole-specific conditions in groundwater from depths of 4 to 450 m in Olkiluoto,

613   Finland. The ISME Journal 2, 760-775.

614   Pedersen, K., Bengtsson, A.F., Edlund, J.S., Eriksson, L.C., 2014. Sulphate-controlled

615   Diversity of Subterranean Microbial Communities over Depth in Deep Groundwater

616   with Opposing Gradients of Sulphate and Methane. Geomicrobiology Journal 31, 617-

617   631.

618   Peters, C.A., Piazolo, S., Webb, G.E., Dutkiewiczc, A., George, S.C., 2016. In search of early

619   life: Carbonate veins in Archean metamorphic rocks as potential hosts of biomarkers.

620   Earth and Planetary Science Letters 453, 44-55.

621   Petersen, H.I., Schovsbo, N.H., Nielsen, A.T., 2013. Reflectance measurements of zooclasts

622   and solid bitumen in Lower Paleozoic shales, southern Scandinavia: Correlation to

623   vitrinite reflectance. International Journal of Coal Geology 114, 1-18.

624   Rasbury, E.T. and Cole, J.M., 2009. Directly dating geologic events: U-Pb dating of

625   carbonates. Reviews of Geophysics, 47(3).

626   Reeburgh, W.S., 2007. Oceanic methane biogeochemistry. Chemical Reviews 107, 486-513.

627   Roberts, N.W., Walker, R.J., 2016. U-Pb geochronology of calcite mineralized faults;

628   absolute dating of rift-related fault events on the northeast Atlantic margin. Geology.

629   Roussel, E.G., Bonavita, M.A., Querellou, J., Cragg, B.A., Webster, G., Prieur, D., Parkes,

630   R.J., 2008. Extending the sub-sea-floor biosphere. Science 320, 1046.

631   Sahlstedt, E., Karhu, J.A., Pitkänen, P., Whitehouse, M., 2016. Biogenic processes in

632   crystalline bedrock fractures indicated by carbon isotope signatures of secondary

633   calcite. Applied Geochemistry 67, 30–41.

634   Sandström, B., Tullborg, E.-L., 2009. Episodic fluid migration in the Fennoscandian Shield

635   recorded by stable isotopes, rare earth elements and fluid inclusions in fracture minerals

636   at Forsmark, Sweden. Chemical Geology 266, 126-142.

637   Sandström, B., Tullborg, E.-L., de Torres, T., Ortiz, J.E., 2006. The occurrence and potential

638   origin of asphaltite in bedrock fractures, Forsmark, central Sweden. GFF 128, 234-242.

639   Schrag, D.P., Higgins, J.A., Macdonald, F.A., Johnston, D.T., 2013. Authigenic Carbonate

640   and the History of the Global Carbon Cycle. Science 339, 540.

641   Schutter, S.R., 2003. Hydrocarbon occurrence and exploration in and around igneous rocks,

642   in: Petford, N., McCaffrey, K.J.W. (Eds.), Hydrocarbons in Crystalline Rocks, pp. 7-33.

643   Segarra, K.E.A., Schubotz, F., Samarkin, V., Yoshinaga, M.Y., Hinrichs, K.U., Joye, S.B.,

644   2015. High rates of anaerobic methane oxidation in freshwater wetlands reduce

645   potential atmospheric methane emissions. Nature Communications 6, 7477.

646   Sherwood Lollar, B., Lacrampe-Couloume, G., Voglesonger, K., Onstott, T.C., Pratt, L.M.,

647   Slater, G.F., 2008. Isotopic signatures of CH4 and higher hydrocarbon gases from

648   Precambrian Shield sites: A model for abiogenic polymerization of hydrocarbons.

649   Geochimica et Cosmochimica Acta 72, 4778-4795.

650   Simoneit, B., 1977. Diterpenoids compounds and other lipis in deep-sea sediments and their

651   geochemical significance. Geochimica et Cosmochimica Acta 41, 463-476.

652   Stevens, T.O., McKinley, J.P., 1995. Lithoautotrophic Microbia, Ecosystems in Deep Basalt

653   Aquifers. Science 270, 450-454.

654   Tazaz, A. M., Bebout, B. M., Kelley, C. A., Poole, J., Chanton, J.P., 2013. Redefining the

655   isotopic boundaries of biogenic methane: Methane from endoevaporites. Icarus 224,

656   268-275.

657   Whiticar, M.J., 1999. Carbon and hydrogen isotope systematics of bacterial formation and

658   oxidation of methane. Chemical Geology 161, 291-314.

659   Wu, X., Holmfeldt, K., Hubalek, V., Lundin, D., Åström, M., Bertilsson, S., Dopson, M.,

660   2016. Microbial metagenomes from three aquifers in the Fennoscandian shield

661   terrestrial deep biosphere reveal metabolic partitioning among populations. The ISME

662   Journal 10, 1192-1203.

663   Zack, T., Hogmalm, J., 2016. Laser ablation Rb/Sr dating by online chemical separation of Rb

664   and Sr in an oxygen-filled reaction cell. Chemical Geology 437, 120-133.

665   Ziegenbalg, S.B., Birgel, D., Hoffmann-Sell, L., Pierre, C., Rouchy, J.M., Peckmann, J.,

666   2012. Anaerobic oxidation of methane in hypersaline Messinian environments revealed

667   by ^{13}C-depleted molecular fossils. Chemical Geology 292-293, 140-148.

668

669 **Figure captions**

670 **Fig. 1.** Mineral appearance. (a) Typical appearance of coarse-grained calcite (white), together

671 with apshaltite (black) and pyrite (metallic cubic crystals) on the fracture surface of a fracture

672 from Forsmark (KFM06C:103 m). (b) SEM-image of intergrowth of a pyrite-calcite aggregate

673 (scalenohedral calcite) on the fracture surface of KAS02:802 m (Laxemar). (c) Scalenohedral

674 calcite intergrown with cubic pyrite, both in an early generation of larger crystals (1) and a

675 later of small cubic crystals (2) intergrown with the outermost growth zone of the calcite

676 crystals (KSH03A:864 m, Laxemar). (d) SEM-image of intergrowth of calcite and adularia

677 (polished crystal cross-section, KLX01:220, Laxemar). (e) SEM-image of a fracture surface

678 coated by the later phase of framboidal pyrite grown on asphaltite and scattered occurrences

679 of late stage calcite and cubic pyrite. Forsmark, KFM01B:24 m. (f) Cubic pyrite crystals

680 intergrown with the outermost calcite growth zone (polished crystal cross-section, KKR02:52

681 m, Götemar).
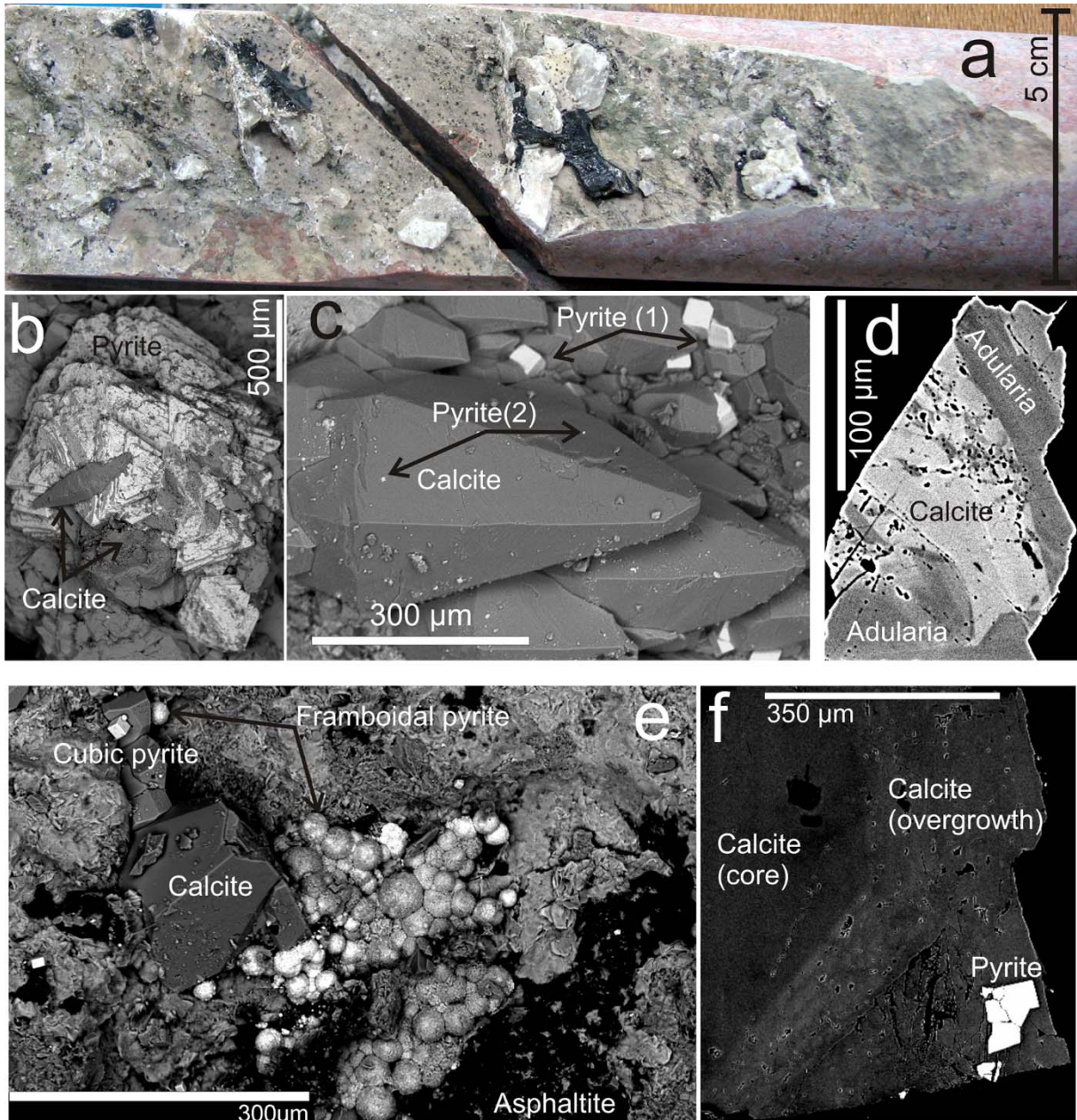
Fig. 2. Stable isotope inventory of calcite. (a-c) Depth distribution of $\delta^{13}C_{calcite}$ from each of the three study areas. Each spot represents one SIMS-analysis. Notable radiometric dating, biomarkers, fossilized microorganisms, and $\delta^{34}S$ values of co-genetic pyrite are also indicated. (d-g) BSE-SEM-images of polished calcite crystals with SIMS analytical $\delta^{13}C$ and $\delta^{18}O$ spot transects below. (d) Crystal showing extremely light $\delta^{13}C$ (-71.3 to -70.5‰) throughout the crystal and $\delta^{18}O$ within -14.0 to -12.8‰, KLX01:220m, Laxemar. (e) Substantially zoned

690   crystal showing two episodes of AOM-related precipitation (δ^{13}C depletion), characterized by

691   different δ^{18}O. Laxemar, KSH03A:863m. (f) Methanogenesis-related δ^{13}C in outermost part

692   of a zoned crystal. Forsmark, KFM05A:110m. (g) Dominantly AOM-related δ^{13}C (-46‰).

693   Forsmark, KFM06C:103m. Distinct difference in isotopic composition and in fluid inclusion

694   signatures between the two calcite phases occurs in this sample (divided by the yellow line).

695   Additional transects are shown in Fig. S3. Error bars are within the size of the symbols

696   (except when shown).

697

698

31
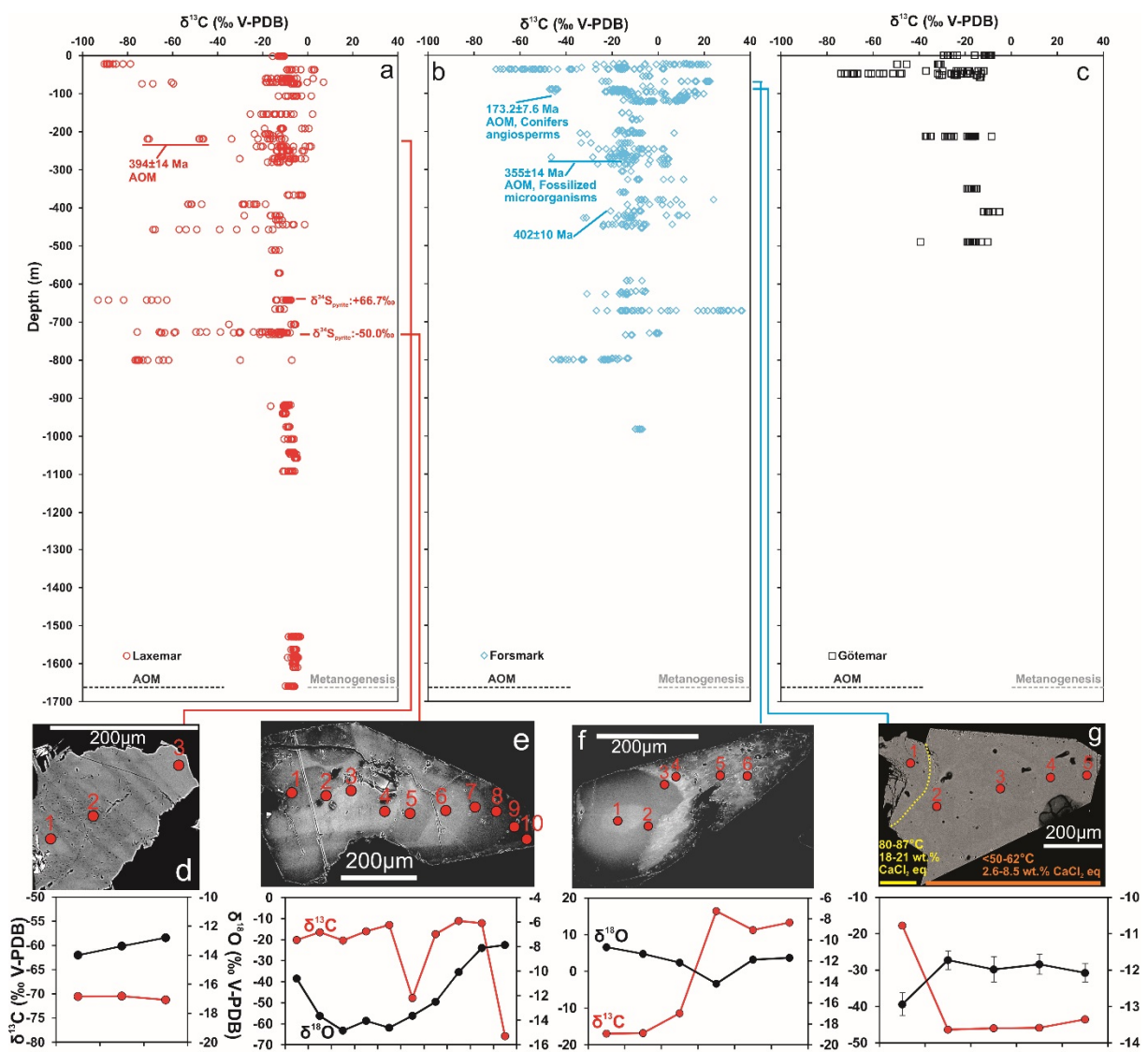
Fig. 3. Direct microscale LA-ICP-MS dating of precipitation phases. (a-c) Rb/Sr isochrons of co-genetic adularia and calcite from (a) KFM04A:306 m, Forsmark (δ^{13}C of calcite has a minimum of -46.3‰) (b) KFM08A:480 m, Forsmark area (δ^{13}C of bulk sample: -21.6‰; Sandström and Tullborg, 2009), (c) KLX01:220 m, Laxemar (δ^{13}C of calcite has a minimum of -70.6‰). Data point ellipses represent 68.3% confidence (the calcite ellipses are too small to be observed in the diagram, as a result of the small error of the ^{87}Sr/^{86}Sr calcite analyses). (b) U-Pb Tera-Wasserburg concordia diagram of calcite sample KFM06C:103 m, Forsmark (this calcite has a minimum δ^{13}C value of -47.1‰).
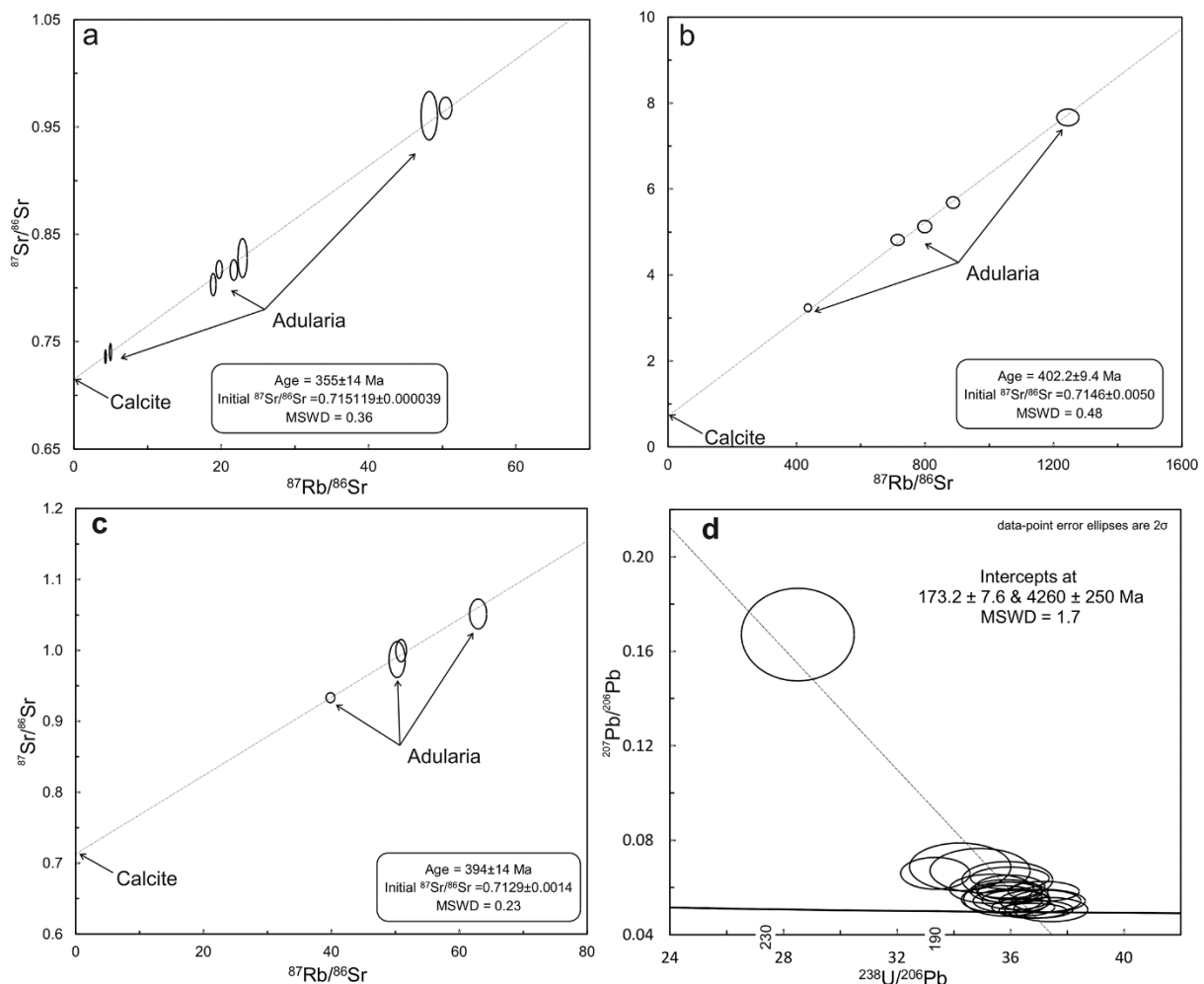
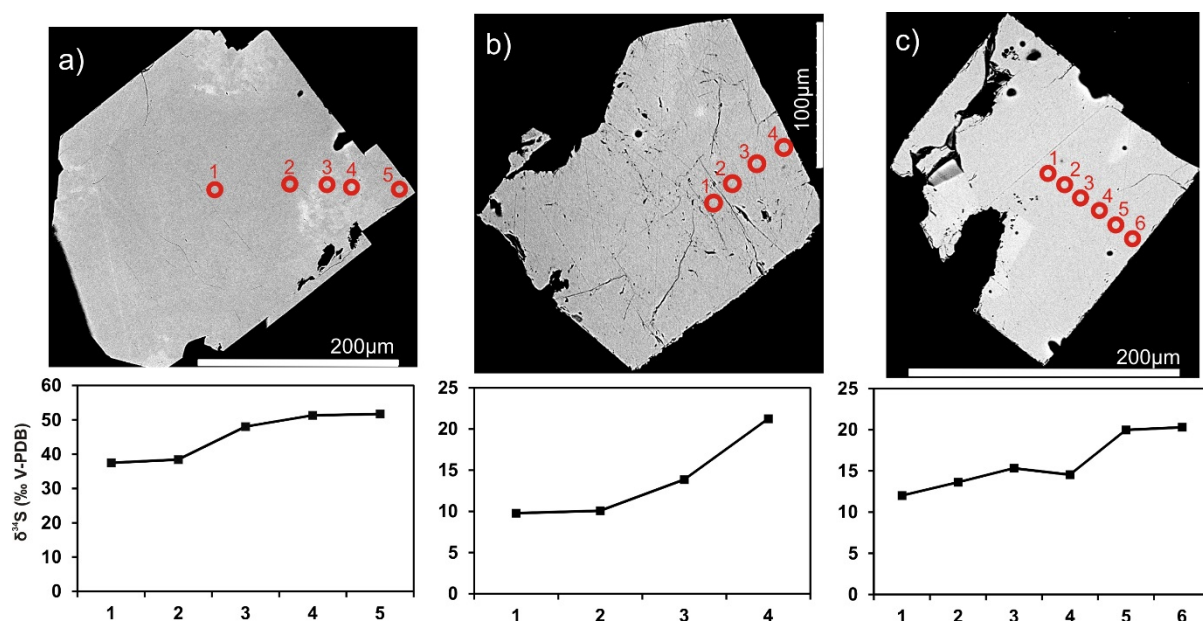**Fig. 4.** S-isotope transects from core to rim of pyrite crystals, showing variable degree of increased δ^{34}S values with growth indicating Rayleigh distillation during bacterial sulfate

711   reduction during semi-closed system conditions. From samples (a) KLX07A:883, (b)

712   KFM08B:43, and (c) KFM06C:103.
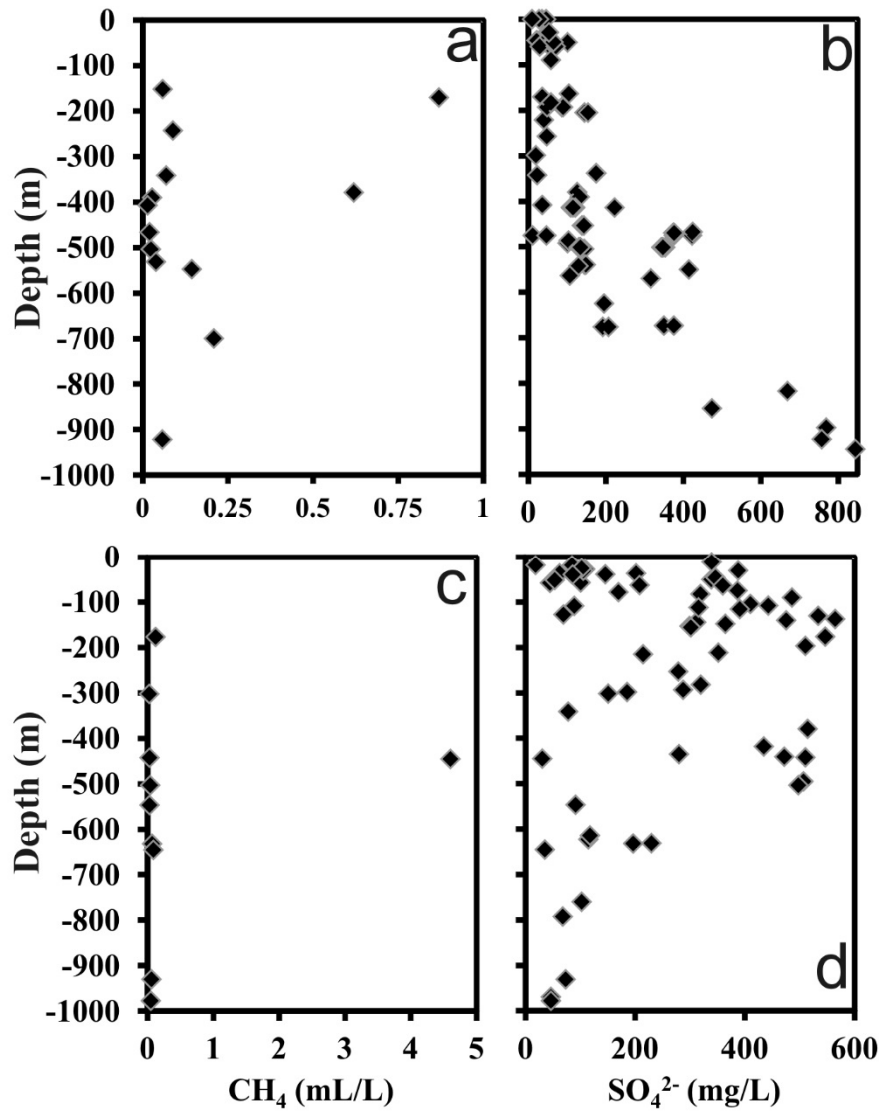

713

714

715   **Fig. 5.** Selected fragmentograms m/z 85 (hydrocarbons) for calcite from KFM06C:103 m

716   (late calcite phase), asphaltite from KFM06C:103 m (related to early calcite phase) and alum

717   shale. The long chain hydrocarbons nC_{22}-C_{35} and diterpenoids (stars) in the calcite from

718   KFM06C:103 m most likely derive from land plants and are not found in the asphaltite or

719   shale. These are clear indicators, that the C in the fluids related to the late stage calcite had a

720   different source than the asphaltite. Organic compounds detected in the calcite sample

721   KFM06C:103 m are listed in Table S9.
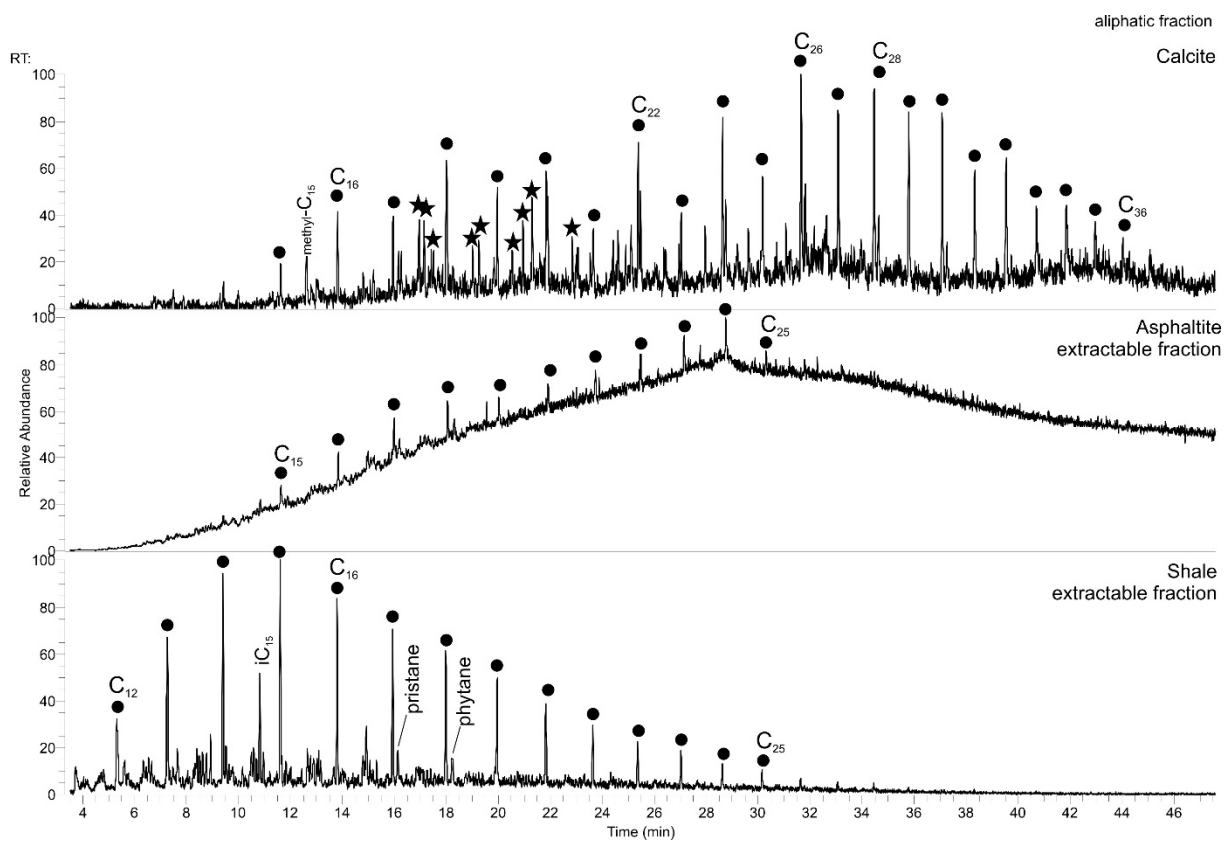
722

723

724   **Fig. 6.** Methane and sulfate concentrations measured in the fracture waters at Laxemar (a,b)

725   and Forsmark (c,d). Data from Drake et al. (2015), Hallbeck and Pedersen (2012), and

726   Laaksoharju et al. (2008).

727